Powder Technology 270 (2015) 141–153

Contents lists available at ScienceDirect

Powder Technology

journal homepage: www.elsevier.com/locate/powtec

On the characterization of size and shape of irregular particles

G.H. Bagheri [a,*], C. Bonadonna [a], I. Manzella [a], P. Vonlanthen [b]

[a] Department of Earth Sciences, University of Geneva, Rue des Maraîchers 13, CH-1205 Geneva, Switzerland
[b] Institute of Earth Sciences, University of Lausanne, UNIL-Mouline, Building Géopolis, CH-1015 Lausanne, Switzerland

ARTICLE INFO

Article history:
Received 24 June 2014
Received in revised form 10 September 2014
Accepted 10 October 2014
Available online 22 October 2014

Keywords:
Irregular particle
Particle shape
Volcanic ash
3D analysis
Image analysis

ABSTRACT

The size and shape characterization of irregular particles is a key issue in many fields of science, which is often associated with large uncertainties. We assess existing protocols and introduce new strategies for the study of size and shape of irregular particles by performing a comprehensive characterization of 127 volcanic clasts with diameters between 155 μm and 37 mm. Methods include caliper measurements, image analysis, laser scanning and scanning electron microscope micro-computed tomography. Volume, surface area and various shape descriptors including form factors (e.g. flatness, elongation), circularity measures and sphericity are analyzed. First, existing procedures commonly applied by caliper and image analysis to determine 1D (i.e. particle lengths in three dimensions) and 2D variables (e.g. particle projection perimeter and area) have been revised. A new procedure based on particle projection area (PA protocol) for measuring particle lengths in three dimensions is also proposed that is associated with the lowest operator-related errors with respect to existing protocols. In addition, the effect of number of particle projections on the variables obtained through image analysis is investigated. It was found that two to three perpendicular projections can be used to characterize 2D variables with a maximum error of <10%. Second, 1D and 2D variables calculated based on the new PA protocol and image analysis are used to derive shape descriptors and investigate their variability and correlations. Finally, both existing and new empirical correlations for the estimation of 3D particle parameters (i.e. volume, surface area, sphericity) based on 1D and 2D variables are presented and benchmarked. It was found that correlations that are based on 2D variables are associated with the lowest average error (~2.6–4.6%).

1. Introduction

Size and shape characterization of particles is of key interest in various fields of science and engineering, including soil and atmospheric sciences, pharmaceutical and food processing, and advanced materials development [1–13]. In volcanology, size and shape of particles play an important role in various processes with large implications for the assessment of hazards, such as dispersion and sedimentation of volcanic particles [12,14–18], reaction of air-borne particles with gases and water vapor in the eruption plume [19], threats to aviation and public health [12,20–24] and geophysical monitoring such as satellite retrievals [25,26].

In order to characterize particle shape several shape descriptors have been introduced over the last few decades. Shape descriptors are mathematical functions that require previous determination of dimensional variables, such as values of length, diameter, perimeter, area or volume. They are here categorized in 1D, 2D and 3D shape descriptors based on the associated methods and variables. A well-known class of 1D shape descriptors called "form factors" that are defined based on the particle lengths in three dimensions (i.e. form dimensions), which can be measured rapidly using a ruler or a caliper. A common example of form factors are flatness and elongation. 2D shape descriptors are based on "2D variables", which are determined through image analysis of particle projections (also called shadowgraphs or silhouettes) [7,9,12,27–32]. Examples of 2D variables typically determined by image analysis are the projection perimeter, area, and diameters of inscribing and circumscribing circles. Traditionally, projections are standard images taken by light microscopes and binoculars. Nowadays modern techniques, such as laser scanning (LS) and computed tomography (CT) can reconstruct external geometry of particles into 3D models that can be used to generate a large number of virtual 2D projections. Sphericity is the only 3D shape descriptor considered in this study, which is defined as the ratio between surface area of a sphere with the same volume as the particle and the surface area of the particle [33]. Sphericity is a measure of the degree to which the shape of a particle approximates that of a true sphere [33,34]. In order to calculate sphericity particle volume and surface area need to be measured using a 3D method, such as 3D laser scanning (LS) and scanning electron microscope micro-computed tomography (SEM micro-CT).

"Form dimensions" used for calculation of "form factors" (e.g. flatness, elongation) consist of three length values, *L*, *I* and *S*, measured along different, usually perpendicular, directions. Several protocols have been established to determine *L*, *I* and *S*. According to the Standard

* Corresponding author. Tel.: +41 22 379 6660.
E-mail address: gholamhossein.bagheri@unige.ch (G.H. Bagheri).

http://dx.doi.org/10.1016/j.powtec.2014.10.015
0032-5910/

(STD) protocol proposed by Krumbein [35], L corresponds to the longest dimension of the particle, I to the longest dimension perpendicular to L, and S to the longest dimension perpendicular to both I and L. In contrast, Blott and Pye [34] defined L, I and S with respect to the longest, intermediate and shortest edge dimensions of the Minimum Bounding Box (MBB) enclosing the particle. The accuracy of these procedures is, however, highly dependent on the ability of the operator to identify the directions along which form dimensions are to be measured. In particular, errors mostly arise from the difficulty to evaluate the perpendicularity relationship between L, I and S [34,36] (STD protocol) and the proportions of the MBB (MBB protocol).

Similar to caliper measurements, image analysis is subject to operator-dependent errors. In particular, results vary as a function of the orientation and number of selected projections. The analysis of a single randomly-selected projection clearly leads to incomplete results. However, it is not yet clear how many projections of an irregular particle are needed in order to guarantee reliable characterization of size and shape. Cauchy [37] showed that accurate calculations of the surface area, SA, of a convex body (i.e. every line segment between two vertices remains inside or on the boundary of the body) from the area of its projections require an infinite number of projections. Laurentini [38] reported that the volume, V, of any polyhedron of n faces can only be reconstructed provided that n^5 random projections are available. In practice, however, the number of projections is often adapted to the quantities to be measured. As an example, calculations of the terminal fall velocity of volcanic ash particles are generally based on one [7,12,17,18] or two [16] projections. Blott and Pye [34] suggested the use of three perpendicular projections to estimate particle sphericity from circularity measures, and Asahina and Taylor [30] and Taylor et al. [9] used 31 and 65 projections, respectively, to calculate the surface area of gravel-sized rock pieces.

1D and 2D variables can be easily obtained from caliper measurements and image analysis. On the other hand, the determination of volume, surface area and sphericity, which are hereafter indicated as 3D parameters, needs more sophisticated instruments (e.g. LS) that are more time consuming and in most cases cannot be applied to a large number of particles. Many studies can be found in the literature that explore the possibility of obtaining 3D parameters from 1D and 2D variables [7,9,29–31,34,37,39–42]. However, a comprehensive investigation on this subject is still needed since most of previous studies did not measure 3D parameters directly and/or their relationships with 1D and 2D were not analyzed in detail.

Shortcomings of existing strategies include i) the difficulty in identifying the perpendicularity among L, I and S, which can generate large operator-dependent errors and ii) the lack of quantification of the dependence of image analysis on the number of irregular-particle projection, which can also generate large errors. Finally, in order to better characterize critical particle parameters (e.g. sphericity), which can help describe important physical processes, such as particle transport and sedimentation, a comprehensive study of shape of highly irregular particles is required. This should include simple (e.g. caliper) to complex (e.g. LS and SEM micro-CT) measurement strategies. The evaluation of 3D parameters (e.g. volume, surface area, sphericity) based on 1D and 2D variables also needs to be investigated in more detail.

In order to address the issues and shortcomings mentioned above, we have carried out a systematic study on 127 volcanic clasts between 155 μm–36 mm, which are good general case studies of irregular particles. Several methods for the characterization of our particles are used, including caliper measurements, image analysis, LS and SEM micro-CT. First, existing procedures commonly applied to determine the variables of shape descriptors are revised (i.e. 1D and 2D variables). In particular, a new protocol, called projection area-based protocol (PA), is proposed for the measurement of form dimensions with low operator-dependent errors. Second, 1D and 2D variables are used to calculate shape descriptors (i.e. form factors, circularity, sphericity). Third, both new and existing empirical correlations are benchmarked for applications where 3D parameters are obtained indirectly from shape descriptors and both 1D and 2D variables.

2. Samples

Selected particles are divided in two sample sets (Table 1) based on the common size classification used in volcanology: lapilli ($2\ \text{mm} < d_{eq} < 64\ \text{mm}$) and ash particles ($d_{eq} < 2\ \text{mm}$), where d_{eq}, obtained from LS and SEM micro-CT measurements, is the equivalent spherical diameter defined as the diameter of the sphere with the same volume V as the particle ($d_{eq} = \sqrt[3]{6\ V/\pi}$).

Sample Set 1 consists of 115 lapilli-sized particles with $11\ \text{mm} < d_{eq} < 36\ \text{mm}$ collected from various tephra deposits, including those of Chaitén (Chile, 2008), Llaima (Chile, 1957), Villarrica (Chile, Chaimilla unit, 3500 BP), Cotopaxi (Ecuador, layer 2, 290 years BP and layer 5, 1180 years BP [43]), Masaya (Nicaragua, Fontana Lapilli, 60 Ka [44]) and Stromboli (Italy, 2007). 65 particles of Sample Set 1 are vesicular (opening diameter of the vesicles corresponding to 5–40% of d_{eq}, with a mode around 10–25%) and 13 particles have non-vesicular surfaces. The term "vesicle" here refers to surface vesicles only and internal vesicles have not been considered. In addition, 37 particles are also wrapped in Parafilm® (a self-sealing, moldable and flexible wax film) to cover the surface vesicles and increase the population of "non-vesicular" samples without changing their macroscopic shape characteristics. LS 3D models of selected lapilli-sized particles are shown in Fig. 1.

Sample Set 2 consists of 12 ash particles with $155\ \mu\text{m} < d_{eq} < 930\ \mu\text{m}$ that includes 3 vesicular and 9 non-vesicular. Because of their small size, these particles were investigated through SEM micro-CT (Fig. 2) instead of LS and image analysis. The small population of ash particles is due to the fact that SEM micro-CT is a time-consuming technique [45], which cannot be applied to a large number of particles [45]. Ash particles were collected from the tephra deposits of Kīlauea (Hawaii, Mystery Unit of Keanakakoi formation, 1790 AD), Chaitén (Chile, 2008) and Masaya (Nicaragua, Fontana Lapilli, 60 Ka [44]).

3. Measurement methods

3.1. LS (laser scanner)

LS enables the external envelope of a particle to be reconstructed in 3D (Fig. 1). The lapilli-sized particles (Sample Set 1) were scanned using the NextEngine Inc. desktop laser scanner with accuracy of ~100 μm and particle volume and surface area were calculated using the ScanStudio HD Pro software (v.1.3.2) delivered with the apparatus. Samples were glued onto a needle-shaped screw, fixed to a self-rotating and tiltable stage, and rotated over 360°. Digital scans of the samples were taken using increments of 45° to 60° depending on the irregularity of the particle shape. This preliminary scan was then inspected visually and completed by additional scans to improve the orientation coverage. The successive scans were later aligned digitally and a mesh of the particle surface was created. In most cases further cleaning and patching of the mesh is necessary to reduce noise and remove artifacts. Acquisition and post-processing took about 2 h on average for each particle. Our preliminary test showed that particles with d_{eq} of 5 mm are the smallest particle size that can be reconstructed by our LS. In order to validate LS measurements, an official table tennis ball (40 mm in diameter) approved by the ITTF (International Table Tennis Federation) was scanned and its surface area and volume calculated from its 3D model. The errors were within 0.5% with respect to the analytical calculations.

3.2. Scanning electron microscope (SEM) micro-CT

SEM micro-CT enables non-destructive 3D reconstruction and characterization of small objects within the chamber of an SEM [46]. The

Table 1
Samples and methods used in this study.

Sample set	Type	No.	d_{eq}	Surface	Measurement methods
1	Lapilli	65	11–36 mm	Vesicular	Caliper, image analysis and LS
	Lapilli	13	15–21 mm	Non-vesicular	
	Lapilli particles wrapped in Parafilm®	37	11–37 mm	Non-vesicular	
2	Ash	3	205–266 μm	Vesicular	Image analysis and SEM micro-CT
	Ash	9	155–930 μm	Non-vesicular	

technique uses the X-rays generated in the SEM chamber when the electron beam is focused on a metal target. The object to be analyzed is placed in front of the X-ray beam and step-wise rotated over an incremental range of angular orientations. Shadow projections of the sample are then collected by an X-ray sensitive camera and used to reconstruct 2D CT slices and 3D models of the object with a resolution in the order of 1 to 3 μm (see Fig. 2).

SEM micro-CT analyses were carried out at the University of Lausanne (Switzerland) using a CamScan MV2300 SEM equipped with a Bruker SEM micro-CT attachment. This device consists of a Princeton Instruments PIXIS XO X-ray camera and a computer-controlled motorized stage. The SEM was operated at 30 kV and 300 nA to maximize the penetration power of X-rays and to increase the signal-to-noise ratio in the shadow projections. Depending on the density, particles with diameters between 0.1 and 1.0 mm can be reconstructed by using our SEM micro-CT. In order to check the accuracy of the method, the form dimensions obtained from SEM micro-CT were compared to the dimensions measured using an optical microscope. Results showed a maximum of 3% deviation. For a detailed description of the SEM micro-CT technique and its applicability to volcanic ash, the reader is referred to Vonlanthen et al. [45].

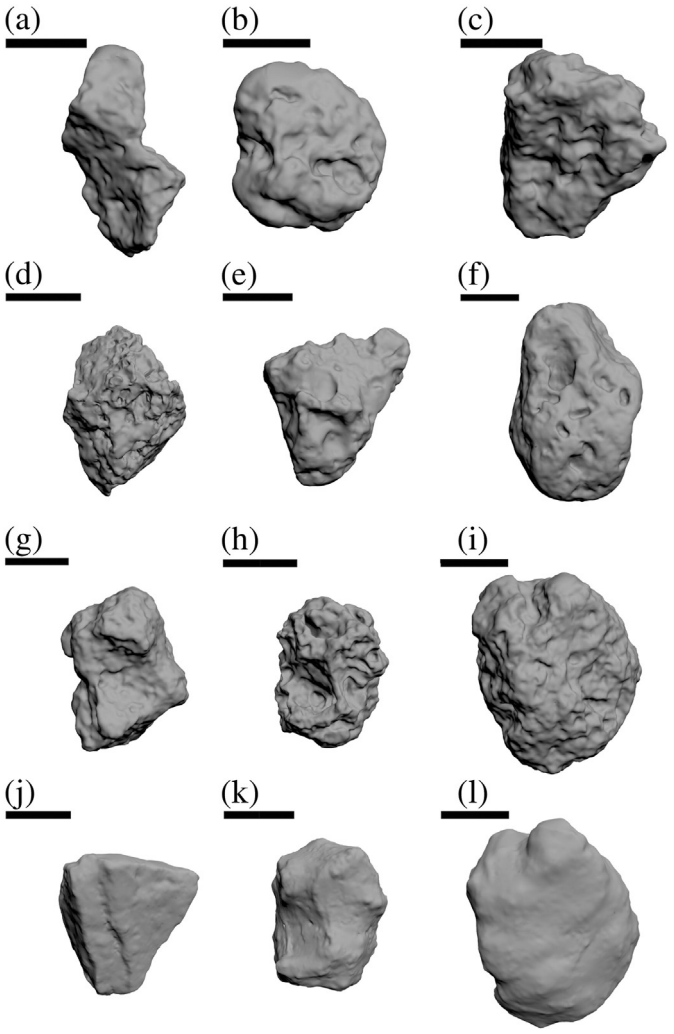

Fig. 1. LS 3D models of selected particles of Sample Set 1 (scale bar: 10 mm). Particles *k* and *l* are Parafilm®-wrapped models of particles *h* and *i*, respectively. Particles *a* to *i* are considered as vesicular and particles *j* to *l* are considered as non-vesicular. Source of particles are as follows: *a* and *c* from Cotopaxi layer 5, *b* from Cotopaxi layer 2, *d* from Villarrica Chaimilla unit, *h* from Llaima 1957, *f* and *l* from Chaitén 2008, *e*, *i* and *g* from Masaya Fontana Lapilli.

3.3. Caliper

A digital caliper with accuracy of 0.01 mm was used to measure form dimensions of particles in Sample Set 1. Because of the impracticality of manipulating small objects, caliper measurements could not be performed on particles of Sample Set 2.

3.4. Image analysis

For each particle, image analyses were performed on 1000 random projections that were extracted from the 3D models obtained from LS and SEM micro-CT. The size of each projection is 1000 × 1000 pixels, which corresponds to spatial resolution of 11 to 36 μm/px for the particles of Sample Set 1 and nominal spatial resolution of 0.2 to 1 μm/px for those of Sample Set 2. Random projections were analyzed using the ImageJ software [47] to extract 2D variables that include the perimeter, P, circle equivalent diameter, d_{2D}, area, A, diameter of the largest inscribed circle, D_i, and diameter of the smallest circumscribed circle, D_c (see Fig. 3). Other than these variables, there are other variables that can be obtained from image analysis, such as minimum and maximum caliper lengths of the projection (i.e. l_{min} and l_{max}). l_{min} and l_{max} can be considered as equivalent to L, I or S depending on the particle orientation in the projection (see Section 5.1.1 for more details). Therefore, they can be used as alternatives for measuring form dimensions since they are associated with less operator-dependent errors compared to those obtained by caliper.

A dedicated FORTRAN code was developed to merge the data obtained from caliper measurement, image analysis, LS and SEM micro-CT and to calculate all shape descriptors. The statistical analysis on the output data from the code was done by the R statistical package [48].

4. Measurement of particle volume and surface area

Depending on the instrument used for measuring volume and surface area of an irregular particle different values might be obtained. In particular, surface area of an irregular porous object is a function of scale and depends on the considered measurement strategy [9]. For example, gas-adsorption methods measure particle surface area down to molecule level while LS and SEM micro-CT work at much higher scales (0.1–1.0% of d_{eq}) [7,12,27]. As a result, surface area and related parameters, such as sphericity, obtained with LS and SEM micro-CT cannot be compared with those obtained from gas-adsorption methods. In this study, in order to have a reference value for 3D parameters, i.e. particle volume (and eventually d_{eq}), surface area (SA) and sphericity (ψ, see

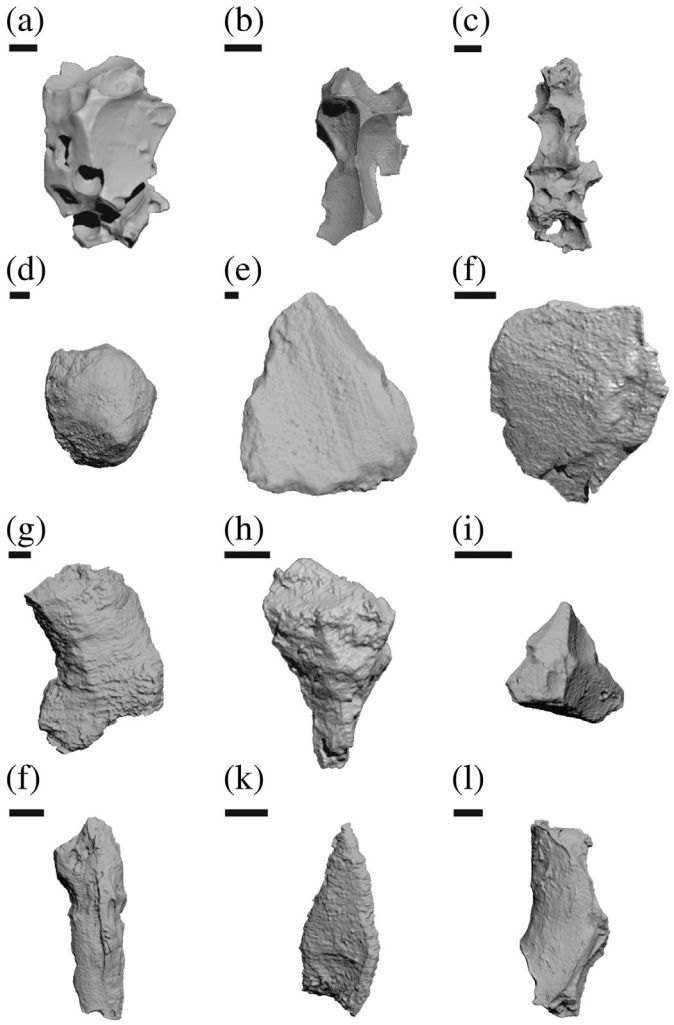

Fig. 2. SEM micro-CT models of the volcanic ash particles of Sample Set 2 (scale bar: 100 μm). Particles *a* to *c* are considered as vesicular and particles *d* to *l* are considered as non-vesicular. Source of particles area as follow: *b*, *d*, *f*, *g*, *h*, *i* and *k* from Kīlauea Mystery Unit of Keanakakoi formation; *a*, *c*, *j* and *l* from Masaya Fontana Lapilli; and *e* from Chaitén 2008.

Table 3 for definition), values obtained from LS and SEM micro-CT are used.

5. Results

5.1. Measuring strategies

5.1.1. Form dimensions: the new projection area (PA) protocol

In order to reduce the operator-dependent errors associated with both the STD and MBB protocols, a new approach based on projection area (PA) is introduced for the measurement of form dimensions (i.e. *L*, *I*, *S*). Unlike the STD and MBB protocols, the PA protocol does not require *L*, *I* and *S* to be measured perpendicularly to each other. Instead, they are measured on two specific projections of the particle, namely the projections with maximum and minimum areas. *L* and *I* are defined as the largest and smallest dimensions measured on the maximum-area projection, and *S* corresponds to the smallest dimension measured in the minimum-area projection. A sketch illustrating the dimensions associated with the STD, MBB and PA protocols is shown in Fig. 4.

In order to test the operator-dependency of the PA protocol, three different operators measured form dimensions of particles shown in Fig. 1 through both the MBB and PA methods by using a digital caliper (Table 2). The application of the MBB protocol with caliper is described by Blott and Pye [34] and shown in Fig. 4b. In contrast, the application of the PA protocol is based on the maximum and minimum projections visually identified by different operators (Fig. 4c). Maximum and minimum dimensions were then measured with a digital caliper. We did not consider the STD method since it is already proven to be highly operator dependent [34,36]. Results show that the PA method is associated with lower operator-dependent errors (1.3–2%) than the MBB method (2.4–5.3%).

In addition, the accuracy of both protocols has been evaluated based on comparison between the caliper measurements and reference form dimensions (Table 2). For the MBB protocol, references consist of the edge dimensions of the Minimum Bounding Box calculated using the MATLAB toolbox [49]. For the PA protocol, references are calculated from the maximum and minimum area projections among 1000 random projections created from 3D models. In order to do so, l_{min} and l_{max} of the maximum projection area of the particle are assigned as *L* and *I*, respectively, and l_{min} of the minimum projection area is assigned as *S*. The average error between measurements and references ranges between 2.8% and 4.6%, with a maximum of 15.1% (for *L*) for the MBB protocol, and between 1.2% and 2.4%, with a maximum of 4.9% (for *I*) for the PA protocol.

The ability of the PA protocol to account for common morphological quantities has been tested in two ways. First, the particle spherical equivalent diameter, d_{eq}, obtained from LS and SEM micro-CT was compared to the averaged geometrical diameter of the equivalent ellipsoid, $d_G = \sqrt[3]{LIS}$, (i.e. an ellipsoid with same tri-axial dimensions as the particle form dimensions). Second, the particle surface area, *SA*, obtained from LS (Sample Set 1) and SEM micro-CT (Sample Set 2) was compared to the surface area of the equivalent ellipsoids, $SA_{ellip.}$. Taylor et al. [9] used the following approximate solution for calculating $SA_{ellip.}$ that is associated with relative error of 0.1% compared to exact results:

$$SA_{ellip.} \approx 4\ \pi \left[\frac{(LI)^{\lambda} + (LS)^{\lambda} + (IS)^{\lambda}}{3 - k\ \left(1 - 27\ LIS\ (L+I+S)^{-3}\right)} \right]^{1/\lambda} \quad (1)$$

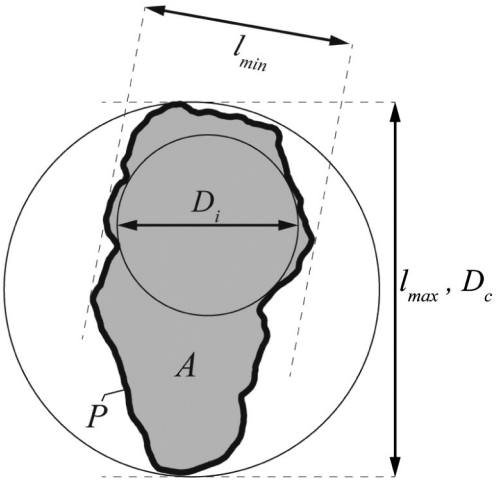

A: Projection area
P: Projection perimeter
$d_{2D} = \sqrt{4A/\pi}$

Fig. 3. Variables determined for a particle projection using ImageJ [47]. The projection shown in this figure is a projection of particle *a* in Fig. 1 that is also its maximum projection area. For each particle in Sample Sets 1 and 2, up to 1000 projections in random orientations of the particle are created from the particle 3D model and analyzed by ImageJ [47]. *A* ≡ projection area, *P* ≡ projection perimeter, d_{2D} ≡ circle equivalent diameter, l_{min} ≡ minimum caliper length, l_{max} ≡ maximum caliper length, D_i ≡ diameter of the largest inscribed circle and D_c ≡ diameter of the smallest circumscribed circle.

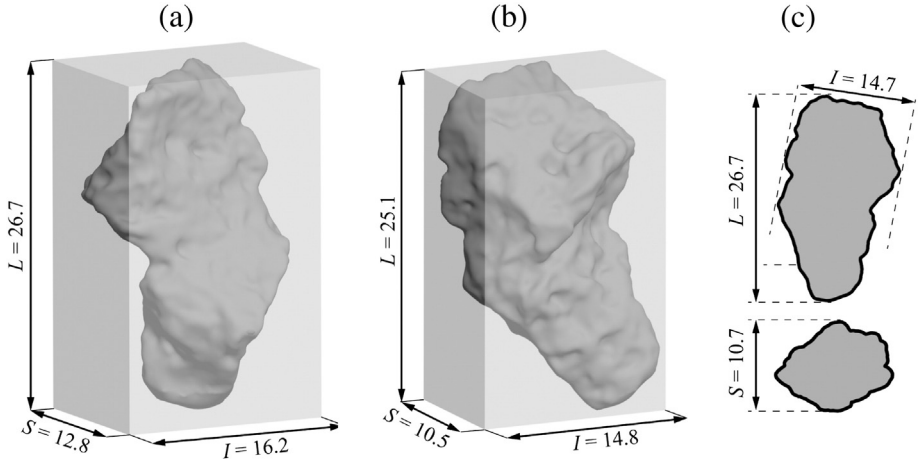

Fig. 4. Schematic illustration of different protocols used to measure form dimensions (L, I and S) of particle a in Fig. 1 (dimensions are in mm). (a) The Standard (STD) protocol proposed by Krumbein [35]; (b) The Minimum Bounding Box (MBB) of Blott and Pye [34] determined using the MATLAB toolbox of Korsawe [49]; (c) Form dimensions inferred from the Projection Area (PA) protocol. Top and bottom projections are the maximum and minimum area projections, respectively.

where $\lambda = 1.5349$, $k = 0.0942$. Fig. 5 shows the ratios of $SA_{ellip.}$ to SA, and of d_G to d_{eq} as boxplots. In each boxplot the ends of the bars represent the smallest and the largest measurements. The box height indicates the first and the third quartiles and the horizontal in the box line is the median (second quartile) of the measurement. The outliers (outside 1.5 times the interquartile range above the upper quartile and bellow the lower quartile) are shown by circles, however, they are not considered for discussion. The number at the bottom of each boxplot is the mean of the distribution. Fig. 5 shows that ratios obtained from the PA protocol are closer to unity and have narrower maximum deviations than those obtained from the MBB protocol. This trend is confirmed by the Pearson correlation coefficient, r, between $SA_{ellip.}$ and SA, and between d_{eq} and d_G. Using the MBB protocol, r values are 0.981 between SA and $SA_{ellip.}$, and 0.987 between d_{eq} and d_G, while they are 0.994 and 0.989, respectively, using the PA protocol.

The use of the new PA protocol can reduce operator-dependent errors for measuring form dimensions of irregular particles (Table 2) and can also provide better estimation of particle volume and surface area (Fig. 5). The PA protocol is also much easier to apply since it is not necessary to maintain the perpendicularity between projections or measured dimensions. The only subjectivity associated with the PA protocol is the choice of maximum and minimum particle projections. In the following sections form dimension of particles are obtained by applying the PA protocol on 1000 random orientation projections. Through this procedure, we make sure that the presented results are not biased by possible operator-dependent errors that might arise from using the caliper.

5.1.2. Image analysis: effect of particle orientation and number of projections

The particle 3D model (obtained from LS or SEM micro-CT) enables the generation of several hundreds of randomly oriented projections. This allows us to determine easily the influence of the number of projections, N, on widely-used 2D variables and shape descriptors: the circle equivalent diameter, d_{2D}, the Riley circularity [50], φ_{Riley}, and the Cox circularity [51], φ_{Cox} (Fig. 6). The definitions of circularity measures are presented in Table 3. The average values of d_{2D}, φ_{Riley} and φ_{Cox} were calculated for each particle for $N = 1, 2, 3, 10, 20, 50, 100$ and 1000. Values that averaged over 1000 projections, shown by overscores (i.e. $\overline{d_{2D}}$, $\overline{\varphi}_{Riley}$, $\overline{\varphi}_{Cox}$), were used as references for the values averaged over $N < 1000$. For $N = 1$ the projection with maximum area was selected since it is the most possible orientation of the particle when its image is taken by microscopes (due to higher stability in such orientations) among other possible orientations. The minimum and maximum area projections were used for $N = 2$, and three perpendicular projections were selected for $N = 3$ (the first being the maximum area projection).

Table 2
Comparisons of the MBB [34] and PA protocols for measuring form dimensions of particles shown in Fig. 1 (Dimensions are in mm). Three different operators (oprs.) made caliper measurements and values in table are mean of their readings. Deviations shown at bottom of caliper readings are the deviation between readings of different operators. Errors presented in the last row are relative errors between average of caliper readings and MATLAB toolbox [49] for the MBB [34]; and caliper readings and image analysis for the PA.

ID	MBB [34]						PA					
	Mean caliper			MATLAB [49]			Mean caliper			Image analysis		
	L	*I*	*S*	*L*	*I*	*S*	*L*	*I*	*S*	*L*	*I*	*S*
a	25.9	15.0	11.0	25.1	14.8	10.5	25.9	15.0	10.6	26.7	14.7	10.7
b	19.6	16.7	13.3	19.5	15.8	13.8	20.1	16.8	13.3	20.4	17.6	13.6
c	25.2	21.2	9.2	25.1	20.8	9.4	26.0	20.8	9.3	26.1	21.1	9.5
d	21.9	16.8	14.9	19.0	16.1	14.5	22.5	15.4	14.5	22.6	16.0	15.1
e	24.7	19.0	12.2	21.7	20.9	12.6	26.1	19.0	12.5	26.2	18.9	12.7
f	34.5	22.0	15.4	33.0	22.9	16.0	34.5	22.6	15.4	34.8	22.5	16.1
g	26.2	18.8	13.5	26.3	18.6	13.6	27.3	19.1	13.6	27.3	18.8	13.7
h, k	19.7	16.2	11.2	20.2	16.5	11.0	20.5	16.5	11.0	21.2	16.5	11.1
i, l	30.2	24.2	16.6	30.6	24.2	18.2	30.9	24.2	17.8	31.1	23.8	17.6
j	32.2	26.1	13.0	32.7	25.4	13.5	32.9	25.4	13.4	32.8	25.7	13.6
Max. dev. oprs. %	*6.5*	*7.4*	*4.6*				*5.0*	*4.4*	*3.9*			
Avg. dev. oprs. %	**2.4**	**5.3**	**2.7**				**1.5**	**1.3**	**2.0**			
Max. Error %				*15.1*	*5.8*	*4.7*				*3.4*	*4.9*	*4.5*
Avg. error %				**4.6**	**2.9**	**2.8**				**1.2**	**2.4**	**2.0**

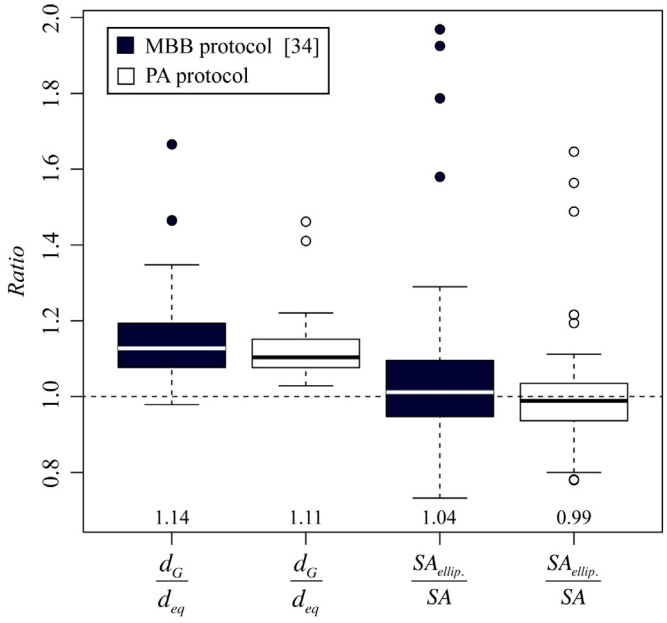

Fig. 5. Box plot showing the variability of ratios of d_G and $SA_{ellip.}$ calculated from the form dimensions (L, I and S) to d_{eq} and SA obtained from LS and SEM micro-CT measurements. Each boxplot shows the distribution of the corresponding ratio within all particles of Sample Sets 1 and 2. Form dimensions were measured using a digital caliper following either the MBB [34] (black boxes) or the PA protocol (white boxes).

For $N > 3$, the three perpendicular projections were completed by randomly selected projections.

Fig. 6 shows that the average of deviations decreases as the number of projections increases. For $N = 1$ the deviation of the median is +12% for d_{2D}, +4% for φ_{Riley}^*, and +1% for φ_{Cox}^* (compared to the value averaged over 1000 projections $N = 1000$, dotted horizontal line). For $N = 2$ the deviation of the median remains constant for φ_{Cox}^*, while it significantly decreases for φ_{Riley} (+2%) and $\overline{d_{2D}}$ (−1%). Whiskers shrink significantly with increasing N (~20% for $N = 1$, 5–8% for $N = 3$, and ~2.5% for $N = 50$).

In summary, a single projection ($N = 1$) is not sufficient to estimate $\overline{d_{2D}}$, but it can estimate $\overline{\varphi}_{Riley}$ and $\overline{\varphi}_{Cox}$ with error distributions centered around zero. Using a large amount of projections ($N > 10$) significantly improves the results. However, acquisition and post-processing time increases when a large number of projections is considered. Using two projections that include minimum and maximum projections ($N = 2$) or three perpendicular projections ($N = 3$) can be considered as the best compromise between time and accuracy.

5.2. Shape descriptors of Sample Set 1 and 2

In the previous section, 1D variables (i.e. form dimensions) of sample particles were obtained through PA protocol and 2D variables by image analysis. In this section various shape descriptors are calculated and the shape characteristics of our sample particles are investigated. In particular, shape descriptors considered in this study are those that are most used in transport and sedimentation studies [52] and are divided in 1D, 2D and 3D descriptors (Table 3). 1D shape descriptors are typically called form factors since they are defined based on form dimensions (i.e. L, I, S). Form factors considered here include: (i) elongation and flatness [53], (ii) Krumbein intercept sphericity [54], (iii) Corey shape factor [55], (iv) Sneed and Folk maximum projection sphericity [1], (v) Aschenbrenner working sphericity [39], (vi) Wilson and Huang shape factor [14]. 2D shape descriptors include circularity measures (i.e. Cox circularity [51] and Riley circularity [50]) that are based on 2D variables obtained through image analysis. Finally, the sphericity [33] that is related to the particle volume and surface area (obtained from LS and SEM micro-CT) is considered as a 3D shape descriptor. There are other types of shape descriptors, such as roundness, irregularity, convexity indexes and surface texture descriptors that are not considered in this study since we are mainly interested in shape descriptors related to transport and sedimentation behavior of particles.

In this section, first variability range of shape descriptors of our sample particles is presented. This gives insights both into shape characteristics of volcanic particles and into the influence of surface vesicularity on the variability of shape descriptors. Second, through a correlation matrix, we investigate how the shape descriptors are related together and explore the possibility of estimating one shape descriptor from another.

5.2.1. Variability

Variability of all the shape descriptors listed in Table 3 is shown in Fig. 7 for both vesicular and non-vesicular particles. 1D shape descriptors cannot be used to distinguish between vesicular and non-vesicular particles since they are formulated based on form dimensions, which are not sensitive to vesicularity. Fig. 7a shows that particles of Sample Set 1 have elongation between 0.51 and 0.91 and flatness between 0.40 and 1.00. According to the classification terminology suggested by Blott and Pye [34], the particles of Sample Set 1 can be classified as "moderately elongate" to "not elongate" and "moderately flat" to "not flat". Out of all 1D shape descriptors, the working sphericity of Aschenbrenner [39], F_{Ac}, has the lowest variability and the highest mean value, whereas Corey [55], F_{Cr}, and Wilson and Huang [14], F_{WH}, shape descriptors have the lowest mean values. The Riley circularity, $\overline{\varphi}_{Riley}$, shows the same range of values for both non-vesicular and vesicular particles. On the other hand, both sphericity, ψ, and Cox circularity, $\overline{\varphi}_{Cox}$, show different values for vesicular and non-vesicular particles with a very narrow overlapping. Sphericity of non-vesicular particles varies between 0.77 and 0.90 while for vesicular particles sphericity is on average 18% less than non-vesicular particles and varies between 0.53 and 0.80. This is due to the fact that vesicular particles have higher surface area compared to non-vesicular particles of the same volume and, as a result, their sphericity is lower (according to sphericity definition in Table 3).

Fig. 7b shows the variability of shape descriptors for Sample Set 2. Form factors have a wide range of variability between 0.25 and 0.90. Particles of Sample Set 2 have elongation between 0.33 and 0.86 and flatness between 0.34 and 0.88. They can be classified as "very elongate" to "not elongate" and "very flat" to "not flat". Similarly to Sample Set 1, values of ψ and $\overline{\varphi}_{Cox}$ are different for non-vesicular and vesicular particles. Sphericity of non-vesicular particles in Sample Set 2 varies between 0.50 and 0.86 while for vesicular particles sphericity is in average 33% less than non-vesicular particles and varies between 0.43 and 0.46. In general, all the shape descriptors of Sample Set 2 have lower average values than those of Sample Set 1.

5.2.2. Correlation between shape descriptors

Correlation matrix between various shape descriptors of Table 3 is shown in Fig. 8. The diagonal elements are symbols of the shape descriptor listed in Table 3. The scatter plots between shape descriptors are shown under the main diagonal and the corresponding Pearson's correlation coefficients, r, are shown above the main diagonal. As an example, a strong linear correlation in the scatter plot between F_{Kr} and F_{WH} can be seen, which is also reflected in the correlation coefficient of 0.99 between these variables.

1D shape descriptors are either affected by the particle elongation or by their flatness. F_{Cr}, F_{SF} and F_{Ac} are highly correlated with each other ($r = 0.93$–1.00) and all of them have high correlation coefficients with the particle flatness ($r = 0.76$–0.91). A similar situation exists between F_{Kr}, F_{WH} and particle elongation. The correlation matrix shows that, as we go from 1D shape descriptors to 2D and then to 3D shape descriptors, the relation between shape descriptors of different dimensions weakens so that there is almost no correlation between

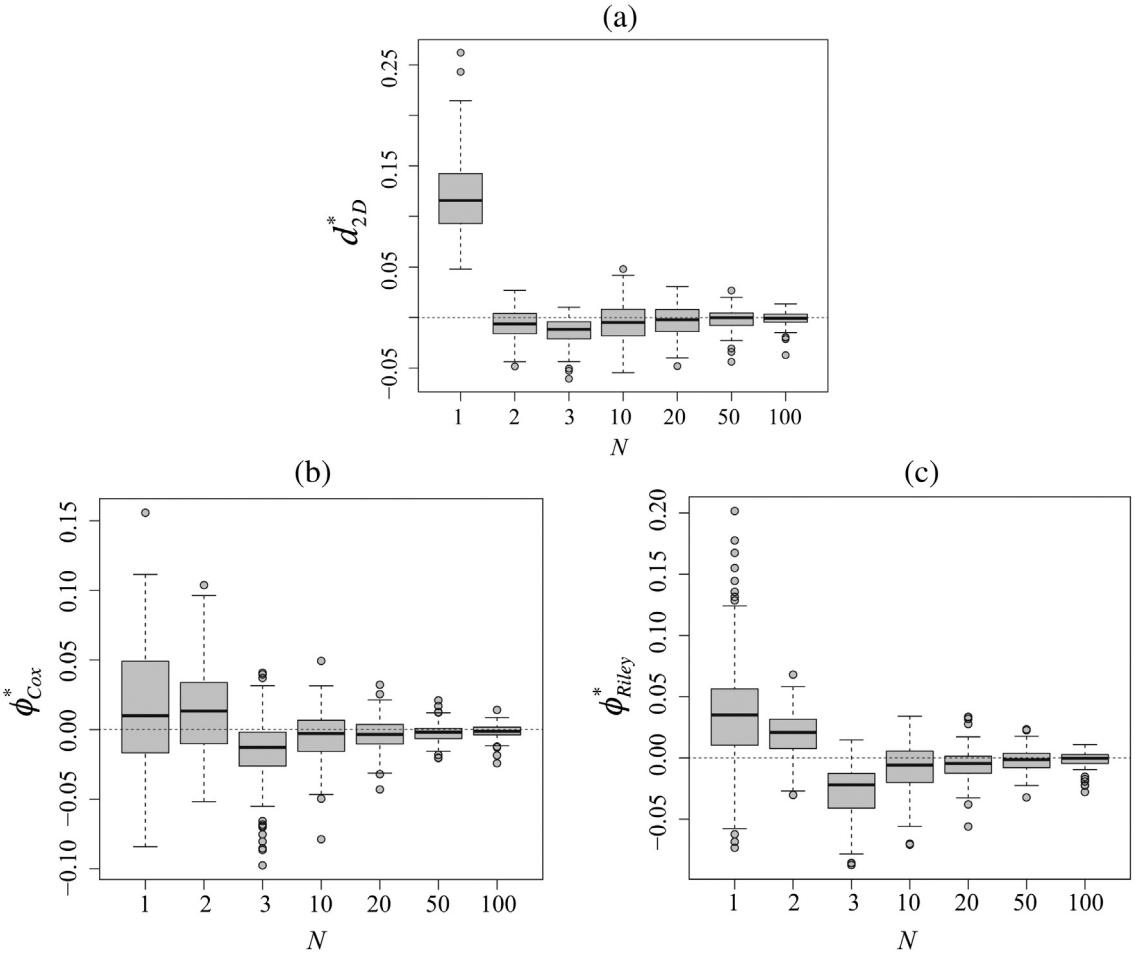

Fig. 6. Influence of number of projections N on the deviation of on the average of (a) circle equivalent diameter d_{2D}, (b) the Cox circularity φ_{Cox} [51], and (c) the Riley circularity φ_{Riley} [50]. For each parameter x (i.e. d_{2D}, φ_{Cox}, φ_{Riley}) the deviation x^* is calculated as $x^* = \left(\left[\sum_{i=1}^{N} x_i \Big/ N\right] - \bar{x}\right) \Big/ \bar{x}$ where $\bar{x}$ is the average over 1000 projections. Each boxplot shows the distribution of the deviation x^* for all particles in Sample Sets 1 and 2.

1D descriptors and sphericity. Among 1D descriptors, F_{Kr} has the highest correlation coefficient with the sphericity and, as shown in Fig. 7, its range of variability is also very close to that of sphericity. But in any case, the correlation between F_{Kr} and sphericity is not significant as it can be seen from their scatterplot. Strong correlations between $\overline{\varphi}_{Riley}$ and most of 1D descriptors, in particular F_{Kr} and F_{WH}, exist. This can be explained by looking at the formulation of $\overline{\varphi}_{Riley}$ $(= \sqrt{D_i/D_c})$ that is defined based on 2D variables that are constrained by 1D variables. In fact, D_c and D_i are constrained by L and S, respectively, and as a result $\overline{\varphi}_{Riley}$ can be roughly approximated by $\sqrt{S/L}$. Interestingly, the correlation between $\overline{\varphi}_{Riley}$ and $\overline{\varphi}_{Cox}$ is not very strong $(r = 0.68)$ although both of them are introduced as measures of circularity. Finally, the sphericity, ψ, has very strong correlation with $\overline{\varphi}_{Cox}$, whereas there is almost no correlation between the particle sphericity and $\overline{\varphi}_{Riley}$. In the next section we discuss in more detail the relationship between sphericity and circularity measures.

Various shape descriptors are measured for both sample sets. All shape descriptors (Fig. 7), imply that the ash particles of Sample Set 2 are more irregular compared to particles of Sample Set 1. This indicates that, at least for the sample sets characterized in this study, shape of volcanic particles is a function of size and irregularity increases with decreasing size. A more definite conclusion could be made if a larger number of ash-size particles were characterized. The decrease for the shape descriptors shown in Fig. 7 between ash and lapilli-size particles is around 5–42%.

5.3. Indirect evaluation of 3D parameters based on 1D and 2D variables

In this section we investigate how results obtained in previous sections can be used for indirect evaluation of 3D parameters (i.e. volume, surface area and sphericity). First, we benchmark existing strategies and then we introduce new strategies that are associated with smaller relative errors and uncertainties. Volume, surface area and sphericity of 3D models (obtained from LS or SEM micro-CT) are considered as the reference values for benchmarking estimations of 1D- and 2D-based strategies.

5.3.1. Existing strategies

5.3.1.1. Volume. In order to estimate particle volume indirectly from 1D or 2D variables, the equivalent spherical diameter of the particle, d_{eq}, should first be estimated. The most used techniques for estimating d_{eq} from 1D variables is to average the particle form dimensions either arithmetically, $d_A = (L + I + S)/3$, or geometrically, $d_G = \sqrt[3]{LIS}$. As mentioned earlier, estimating d_{eq} by d_G is equivalent to estimating particle volume by volume of the equivalent ellipsoid. For estimating d_{eq} from 2D variables, a common method is to use the circle equivalent diameter that is averaged over multiple projections, $\overline{d_{2D}}$ [9,29–31,42]. However, in some applications only a single projection of the particle obtained from microscope is used to estimate $\overline{d_{2D}}$ [7,17,18]. Therefore, in addition to $\overline{d_{2D}}$, we also consider the circle equivalent diameter of particles obtained

Table 3
Shape descriptors measured for each particle. Shape descriptors are categorized based on the classification proposed by Blott and Pye [34] and, therefore, might differ from that of original papers (for more details please refer to Blott and Pye [34]).

Formula	Notes
Form factors (1D)	
$e = I/L$	Elongation [52]
$f = S/I$	Flatness [52]
$F_{Kr} = \sqrt[3]{IS/L^2}$	Krumbein intercept sphericity [53]
$F_{Cr} = S/\sqrt{LI}$	Corey shape factor [54]
$F_{SF} = \sqrt[3]{S^2/LI}$	Sneed and Folk maximum projection sphericity [1]
$F_{Ac} = \frac{12.8\sqrt[3]{f^2 e}}{1+f(1+e)+6\sqrt{1+f^2(1+e^2)}}$	Aschenbrenner working sphericity [39], is sphericity of a tetrakaidekahedron derived from its flatness and elongation
$F_{WH} = (I + S)/2\ L$	Wilson and Huang shape factor [14] for estimating drag coefficient of irregular volcanic particles
Circularity measures (2D)	
$\varphi_{Cox} = 4\pi A/P^2$	Cox circularity (Cox [51] called it roundness)
$\varphi_{Riley} = \sqrt{D_i/D_c}$	Riley circularity (Riley [50] called it inscribed circle sphericity)
Sphericity (3D)	
$\psi = \pi d_{eq}^2/SA$	Sphericity [33]

from their maximum area projection, max(d_{2D}), as another common estimator for d_{eq}.

In Fig. 9 ratios of d_A, d_G, max(d_{2D}) and $\overline{d_{2D}}$ to the reference d_{eq} versus particle sphericity for both sets of particles are shown. Interestingly, all ratios are greater than one, which indicates that in all cases d_{eq} is overestimated (up to 80%) by parameters based on 1D or 2D variables. On average the overestimation of d_A is 16%, of max(d_{2D}) is 26% and values of both d_G and $\overline{d_{2D}}$ are on average 12% higher than d_{eq}. However, if more particles with sphericity lower than 0.5 existed in our sample, the average of overestimation could be higher. The general trend in Fig. 9 shows that the overestimation is strongly dependent on the particle sphericity so that, as the particle sphericity increases, the overestimation decreases. For each parameter a non-linear curve is fitted and their coefficients of determination, R^2, are shown on the plot. Slope of fitted curves indicate that ratios of d_A and max(d_{2D}) to d_{eq} are more affected by the particle sphericity than those of d_G and $\overline{d_{2D}}$.

5.3.1.2. Surface area (SA). The common method for estimating *SA* from 1D variables is the surface area of an ellipsoid with the same form dimensions as the particle, as shown in Eq. (1) [9,16,40]. Taylor et al. [9] found that the *SA* of crushed granite rocks obtained from X-ray CT are on average 10% higher than $SA_{ellip.}$. In the case of volcanic particles, Dellino et al. [16] directly used $SA_{ellip.}$ for estimating surface area of lapilli-sized particles (2–64 mm) whereas Ersoy et al. [28] found $SA_{ellip.}$ to be inadequate for estimating surface area of volcanic ash ($d_{eq} < 125$ μm).

Among approaches based on 2D variables, Cauchy's theorem [37] is the most used method for estimating particle surface area [9]. Cauchy [37] proved that the actual surface area of a convex body is equal to four times the average of projected areas:

$$SA_{Cauchy} = \pi \overline{d_{2D}}^2 \quad (2)$$

A particle is convex if every line segment between two vertices remains inside or on the boundary of the particle. Later, Underwood [56] proved that for non-convex bodies Cauchy's method is the minimum bound. Therefore, any deviation between results obtained by Cauchy's method and actual surface area of particles can be interpreted as a non-convexity measure.

In this study, both $SA_{ellip.}$ and SA_{Cauchy} are calculated for particles of Sample Set 1 and 2 and compared against reference *SA* (Fig. 10). Data points of $SA_{ellip.}/SA$ are scattered around 1.0 with a weak correlation with the particle sphericity. The fitted curve for $SA_{ellip.}/SA$ indicates that in most cases when the particle sphericity is less than 0.8, $SA_{ellip.}$ underestimates surface area and when sphericity is greater than 0.8, it overestimates surface area. On the other hand, the ratio of SA_{Cauchy}/SA is always less than 1.0, which is a sign of non-convexity of volcanic particles [56].

5.3.1.3. Sphericity. Results presented in Figs. 7 and 8 show that the particle sphericity is sensitive to surface vesicularity and, therefore, 1D shape descriptors are not good candidates for estimating particle sphericity. 2D shape descriptors, on the other hand, are sensitive to the particle vesicularity and therefore are better candidates for the estimation of sphericity. In particular, the Cox circularity [51], $\overline{\varphi}_{Cox}$, has a strong correlation with the particle sphericity (Fig. 8). Using circularity measures

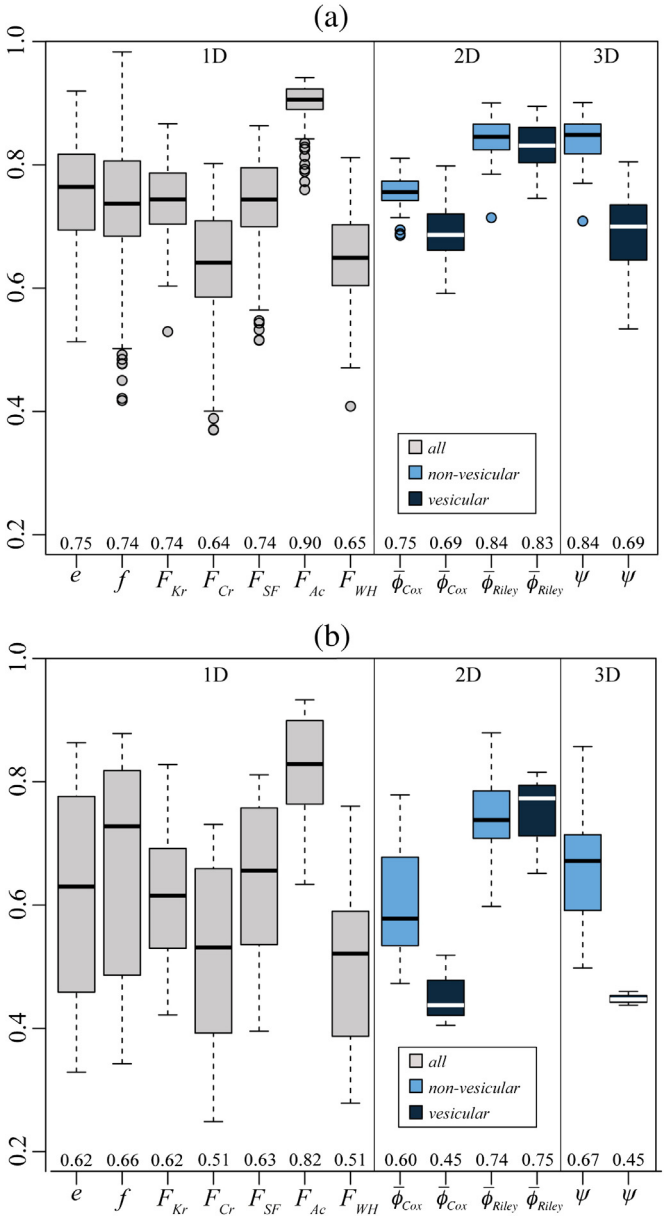

Fig. 7. Distributions of the shape descriptors listed in Table 3 for the particles of (a) Sample Set 1 and (b) Sample Set 2. $\overline{\varphi}_{Riley}$ and $\overline{\varphi}_{Cox}$ are obtained by averaging φ_{Riley} and φ_{Cox} over 1000 projections. The number at the bottom of each boxplot is the mean of the distribution. Regarding 1D shape descriptors, no distinction could be made between particles with vesicular and non-vesicular surface texture since they are formulated based on form dimensions (*L*, *I* and *S*) that are not sensitive to vesicularity.

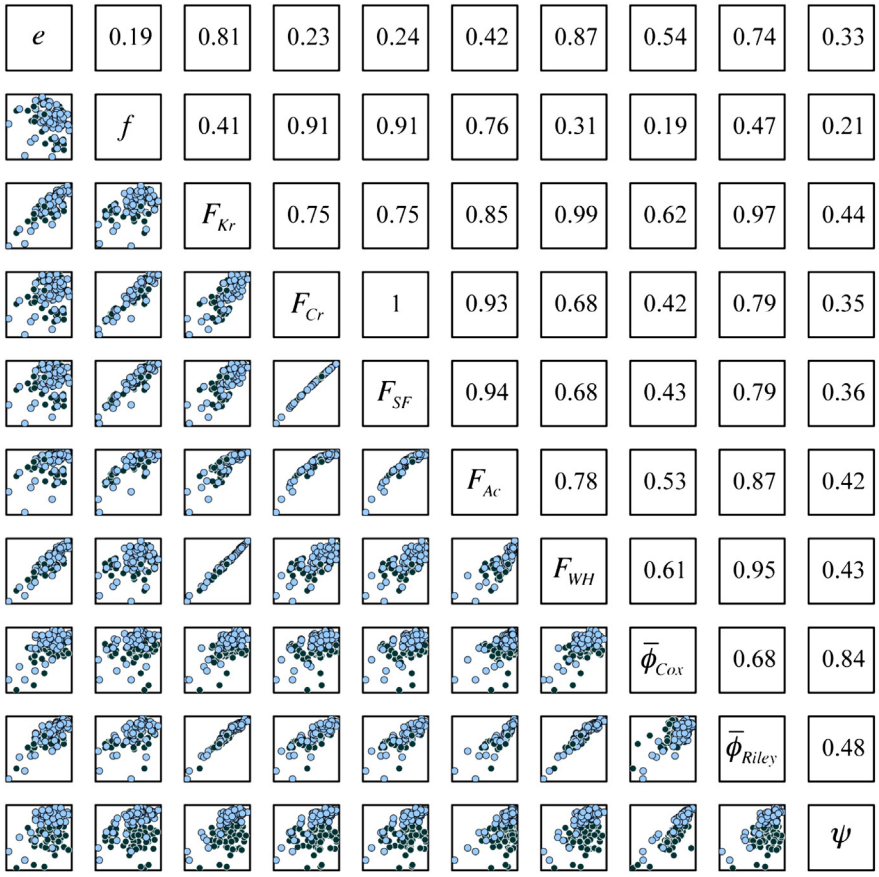

Fig. 8. Correlation matrix of shape descriptors listed in Table 3 for both sample sets. $\overline{\varphi}_{\text{Riley}}$ and $\overline{\varphi}_{\text{Cox}}$ are obtained by averaging φ_{Riley} and φ_{Cox} over 1000 projections. Data corresponding to particles with vesicular and non-vesicular surface are shown by dark and light colors, respectively.

for estimating the sphericity is also suggested by Blott and Pye [34]. They proposed that the Riley circularity [50], $\overline{\varphi}_{\text{Riley}}$, is the best to be used for estimating the particle sphericity since it is simple to calculate and its estimation is in agreement with another circularity index proposed by Wadell [57].

Fig. 11 shows the variation of sphericity obtained from LS and SEM micro-CT with respect to $\overline{\varphi}_{\text{Riley}}$ and $\overline{\varphi}_{\text{Cox}}$ obtained by image analysis. In Fig. 11, $\overline{\varphi}_{\text{Riley}}$ points are scattered and have a weaker correlation with the particle sphericity. Compared to $\overline{\varphi}_{\text{Riley}}$, $\overline{\varphi}_{\text{Cox}}$ is less scattered and has strong positive correlation with the particle sphericity. However,

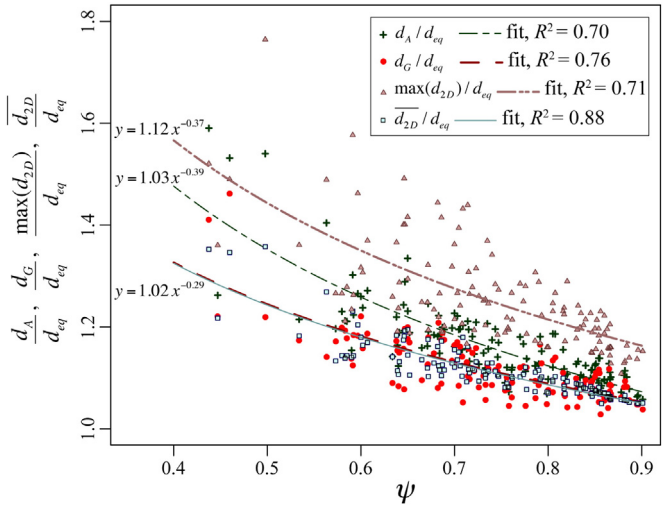

Fig. 9. Ratios of d_A $(=(L+I+S)/3)$, d_G $(=\sqrt[3]{LIS})$, $\max(d_{2D})$ and $\overline{d_{2D}}$ to d_{eq} versus sphericity, ψ. d_{eq} and ψ are obtained from LS and SEM micro-CT measurements. For each parameter, a power-law curve is fitted and the associated coefficient of determination, R^2, is shown.

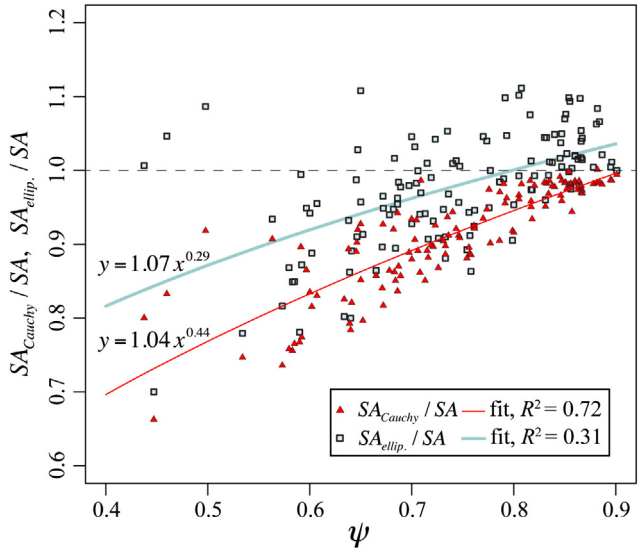

Fig. 10. Ratios of $SA_{\text{ellip.}}$ (Eq. (2)) and SA_{Cauchy} (Eq. (3)) to SA versus sphericity, ψ. SA and ψ are obtained from LS and SEM micro-CT measurements. For each parameter, a power-law curve is fitted and the associated coefficient of determination, R^2, is shown.

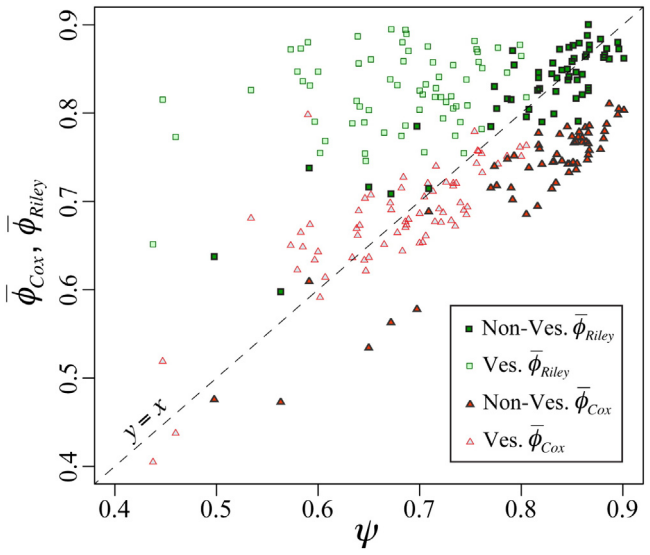

Fig. 11. The variation of Cox circularity [50], $\overline{\varphi}_{Cox}$, and Riley circularity [50], $\overline{\varphi}_{Riley}$, obtained by image analysis versus sphericity, ψ, obtained from LS and SEM micro-CT measurements. $\overline{\varphi}_{Riley}$ and $\overline{\varphi}_{Cox}$ are obtained by averaging φ_{Riley} and φ_{Cox} over 1000 projections.

in general, none of circularity measures is good for estimating sphericity of both vesicular and non-vesicular particles, since $\overline{\varphi}_{Riley}$ overestimates sphericity of vesicular particles and $\overline{\varphi}_{Cox}$ underestimates sphericity of non-vesicular particles. The best estimations for sphericity are $\overline{\varphi}_{Riley}$ for non-vesicular particles and $\overline{\varphi}_{Cox}$ for vesicular particles.

5.3.2. New strategies

In previous section it was shown that existing strategies for estimating particle volume and surface area could be improved if particle sphericity is taken into account. Sphericity can be best constrained when the characteristics of the particle surface are considered, e.g. vesicularity. As a result, new strategies are separately introduced for each category of vesicular and non-vesicular particles (Table 4 and Fig. 12). First, we provide correlations based on only 1D variables, as they are the simplest to obtain. Then we investigate how accurate 3D parameters can be estimated by using various combinations of 1D and 2D variables.

Table 4
Summary of new correlations obtained in the present study for estimating 3D parameters from 1D and 2D variables. Presented notes in this table indicate how the equations are combined together in order to perform the error analysis shown in Fig. 12. All 2D-related parameters (e.g. $\overline{d_{2D}}$, SA_{Cauchy}, φ_{Riley}, φ_{Cox}) needed for error analysis of Eqs. (6*), (7*), (9), (10*) and (11*) are obtained from a single projection (i.e. the maximum projection area).

Eq.	Formula	Type	Notes
Spherical equivalent diameter (d_{eq})			
(3)	$\begin{cases} 0.928\ d_G & \text{non-ves.} \\ 0.887\ d_G & \text{ves.} \end{cases}$	1D	
(7)	$d_G/1.022\ \psi^{-0.29}$	1/2D	ψ from Eq. (6)
(7*)	$d_G/1.022\ \psi^{-0.29}$	1/2D	ψ from Eq. (6*)
(8)	$\overline{d_{2D}}/1.022\ \psi^{-0.29}$	2D	ψ from Eq. (6)
(9)	$max\ (d_{2D})/1.119\ \psi^{-0.37}$	2D	ψ from Eq. (6*)
Surface area (SA)			
(4)	$\begin{cases} 0.995\ SA_{ellip.} & \text{non-ves.} \\ 1.094\ SA_{ellip.} & \text{ves.} \end{cases}$	1D	
(10)	$\pi\ d_{eq}^2/\psi$	2D	ψ from Eq. (6), d_{eq} from Eq. (8)
(10*)	$\pi\ d_{eq}^2/\psi$	2D	ψ from Eq. (6*), d_{eq} from Eq. (9)
(11)	$SA_{Cauchy}/1.044\ \psi^{-0.44}$	2D	ψ from Eq. (6)
(11*)	$SA_{Cauchy}/1.044\ \psi^{-0.44}$	2D	ψ from Eq. (6*)
Sphericity (ψ)			
(5)	$\begin{cases} \pi\ (d_{eq})^2/SA & \text{non-ves.} \\ \pi\ (d_{eq})^2/SA & \text{ves.} \end{cases}$	1D	d_{eq} from Eq. (4) and SA from Eq. (4)
(6)	$\begin{cases} \overline{\varphi}_{Riley} & \text{non-ves.} \\ \overline{\varphi}_{Cox} & \text{ves.} \end{cases}$	2D	$\overline{\varphi}_{Riley}$ and $\overline{\varphi}_{Cox}$ are obtained by averaging φ_{Riley} and φ_{Cox} over 1000 projections
(6*)	$\begin{cases} \varphi_{Riley} & \text{non-ves.} \\ \varphi_{Cox} & \text{ves.} \end{cases}$	2D	φ_{Riley} and φ_{Cox} are obtained from a single projection (i.e. the maximum area projection)

5.3.2.1. Evaluation of 3D parameters based on 1D variables only. Sphericity cannot be well constrained only based on 1D variables as vesicularity requires a 2D or 3D shape descriptors (Fig. 8). Therefore simple linear curve fitting is the most straightforward solution for estimating d_{eq} from d_G, and SA from $SA_{ellip.}$:

$$d_{eq} = \begin{cases} 0.928\ d_G & \text{non-vesicular particles} \\ 0.887\ d_G & \text{vesicular particles} \end{cases} \quad (3)$$

$$SA = \begin{cases} 0.995\ SA_{ellip.} & \text{non-vesicular particles} \\ 1.094\ SA_{ellip.} & \text{vesicular particles} \end{cases} \quad (4)$$

The best estimation of sphericity based on 1D variables is derived from the sphericity definition summarized by Eqs. (3) and (4):

$$\psi = \begin{cases} \pi\ (0.928\ d_G)^2 \Big/ \left(0.995\ SA_{ellip.}\right) & \text{non-vesicular particles} \\ \pi\ (0.887\ d_G)^2 \Big/ \left(1.094\ SA_{ellip.}\right) & \text{vesicular particles} \end{cases} \quad (5)$$

The relative error associated with Eqs. (3) to (5) are shown with boxplots in Fig. 12. The lowest average error is for d_{eq} and the highest is for sphericity. In summary, maximum error by neglecting outliers is less than 10% for estimating d_{eq} and less than 20% for estimating SA and ψ. It is important to mention that most outliers in the corresponding boxplot of Eq. (5) are related to vesicular particles.

5.3.2.2. Evaluation of 3D parameters based on 1D and/or 2D variables. Figs. 9 and 10 showed that estimating d_{eq} and SA from 1D and 2D variables is highly correlated with sphericity. Therefore, if we want to estimate 3D parameters from 1D and/or 2D variables we should start with the sphericity. In the previous section, Eq. (5) is presented for estimating particle sphericity only based on 1D variables that is associated with maximum error of less than 20% and outliers with errors up to 50%. However, in Figs. 8 and 11 it was shown that sphericity could be estimated better from 2D circularity measures than from 1D shape descriptors. In particular, $\overline{\varphi}_{Riley}$ gives the best results for sphericity of non-vesicular particles, while $\overline{\varphi}_{Cox}$ is best for estimating sphericity of vesicular particles (Fig. 11), which is:

$$\psi = \begin{cases} \overline{\varphi}_{Riley} & \text{non-vesicular particles} \\ \overline{\varphi}_{Cox} & \text{vesicular particles} \end{cases} \quad (6)$$

where vesicular particles are, as mentioned in Section 2, those covered with vesicles with opening diameter of the corresponding to 5–40% of d_{eq}, with a mode at around 10–25%, otherwise they are considered as non-vesicular. For error analysis of the correlations presented in this section two scenarios are considered: when 1000 projections are used, $N = 1000$, and when only the maximum area projection of the particle is used, $N = 1$, for calculating 2D variables (in latter case the boxplot label is marked by "*"). For Eq. (6), sphericity estimations have an average error of 4.6% while the average error of Eq. (6*) (see the definition in Table 4) is 7.6% (see Fig. 12). In any case, the maximum errors associated with Eqs. (6) and (6*) are lower than that of Eq. (5).

For estimating d_{eq} the following equations can be written based on curve fits found in Fig. 9:

$$d_{eq} = \frac{d_G}{1.022\ \psi^{-0.29}} \quad (7)$$

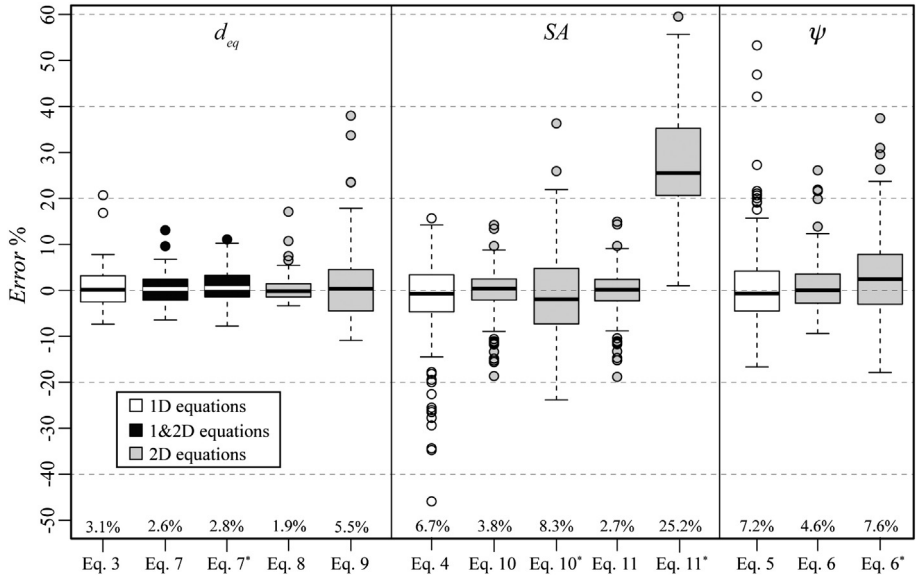

Fig. 12. Distribution of relative errors for estimating spherical equivalent diameter, d_{eq}, surface area, SA, and sphericity, ψ, of particles by using Eqs. (3)–(11) (See Table 4 for details). Relative error, Error %, is defined as (estimation − reference) × 100/reference, where reference values for d_{eq}, SA and ψ are obtained from LS and SEM micro-CT measurements. Numbers at the bottom of boxplots are the absolute mean of Error% ($= \overline{|\text{Error}\,\%|}$).

$$d_{eq} = \frac{\overline{d_{2D}}}{1.022\ \psi^{-0.29}} \tag{8}$$

$$d_{eq} = \frac{max\ (d_{2D})}{1.119\ \psi^{-0.37}} \tag{9}$$

In Eqs. (7) and (8) ψ is estimated from Eq. (6) and in the case of Eqs. (7*) and (9), where only a single projection is considered to be available for calculating 2D variables, ψ is estimated from Eq. (6*). Fig. 12 shows that the lowest average error of 1.9% for estimating d_{eq} of particles of Sample Sets 1 and 2 is obtained by using Eq. (8). The associated average error of Eq. (7) is 2.6% that is not significantly higher than that of Eq. (8). In the case of Eq. (7*) (see the definition in Table 4), where just a single projection of the particle is used for estimating ψ, an average error of 2.8% is obtained that is comparable to that of Eq. (7). The highest estimation error is associated with Eq. (9) that is on average 5.5%. This can be explained by the fact that in Eq. (9) both $max(d_{2D})$ and sphericity are calculated from a single projection. However, an average error of 5.5% is a significant improvement compared to the average error of 26% found when d_{eq} is directly estimated by $max(d_{2D})$ (see Fig. 9).

Particle surface area is estimated from several methods. The first method is to use the sphericity definition (Table 3) to calculate surface area based on sphericity and d_{eq}:

$$SA = \frac{\pi d_{eq}^2}{\psi} \tag{10}$$

The second option is to use curve fits shown in Fig. 10 for improving the estimations of $SA_{ellip.}$ and SA_{Cauchy}. However, $SA_{ellip.}$ estimations cannot be improved by sphericity since the correlation between $SA_{ellip.}/SA$ and sphericity is very weak. On the other hand, SA_{Cauchy}/SA has a strong correlation with sphericity and using sphericity as the second parameter can significantly improve estimations of Cauchy's method:

$$SA = \frac{SA_{Cauchy}}{1.044\ \psi^{-0.44}} \tag{11}$$

In Eqs. (10) and (11), ψ is estimated from Eq. (6) and d_{eq} from Eq. (8). For Eqs. (10*) and (11*) (see the definitions in Table 4), i.e. where a single projection is considered, ψ is estimated from Eq. (6*) and d_{eq} is calculated from Eq. (9) since it is originally derived based on a single projection. Fig. 12 shows that results obtained from Eq. (11) have the lowest average error, i.e. 2.7%. On the other hand, Eq. (11*) is associated with an average error of ~25% and maximum error of 60%. After Eq. (11), Eq. (10) is associated with the lowest value of average error (3.8%). If only a single projection is used for calculating 2D variables, Eq. (10*) with an average error of 8.3% performs significantly better than Eq. (11*).

All equations shown in Fig. 12 and the way they are implemented for error analysis are summarized in Table 4. The objective of presenting various correlations in this study is not just to evaluate which is the most reliable model, but also to provide useful information for applications where particle characterization is limited to a few number of inputs, such as 2D variables obtained only from a single projection. In such applications, the error analysis presented in Fig. 12 clarifies the uncertainty associated with different methods. It is important to note that the obtained correlations (especially correlations based on 1D/2D and 2D variables) might be also used for characterization or firsthand estimations of size and shape of irregular and non-volcanic particles especially if they are non-convex particles.

6. Discussion and conclusions

Size and shape of 127 irregular volcanic particles of various origins and textural properties were characterized using caliper, LS, SEM micro-CT and image analysis. This is the first study that characterizes size and shape of volcanic particles in a wide range of size (155 μm to 36 mm) and based on a wide range of measurement strategies. Particles characterized in this study are also good general case studies of irregular particles and, therefore, all results have fundamental implications for the description of particle transport and sedimentation in various environments, e.g. particle fallout and dispersal during volcanic eruptions, river sedimentations and aerosol dispersal. Based on our results the following conclusions can be drawn for the characterization of irregular particles:

- The PA (projection area) protocol introduced in this study for measuring form dimensions (i.e. L, I, S) is associated with the lowest operator-related errors with respect to existing protocols and associated form

dimensions perform better for both the correlation and estimation of particle volume and surface area. In addition, the PA protocol is much easier to apply since it is not necessary to maintain the perpendicularity between projections or measured dimensions.

- The use of two (i.e. minimum and maximum area) or three perpendicular particle projections for measuring 2D variables was found to be the best compromise between analysis time and accuracy (maximum error compared to when 1000 projections are used is <10%).
- Particle sphericity ψ represents an important parameter for indirect evaluation of particle volume and surface area based on 1D and 2D variables (Figs. 9 and 10). As a result, if indirect and reliable evaluations of particle volume and surface area are needed, particle sphericity should be evaluated first. However, none of existing 1D shape descriptors (e.g. Aschenbrenner working sphericity [39], Sneed and Folk maximum projection sphericity [1]) have strong correlations with the sphericity (Fig. 8). If only 1D variables are available, Eq. (5) can be used for estimating sphericity that is associated with average error of 7.2% and maximum errors up to 20% (Fig. 12). More accurate sphericity estimations can be achieved by using 2D circularity measures (i.e. $\overline{\varphi}_{\text{Riley}}$ and $\overline{\varphi}_{\text{Cox}}$) since they are highly correlated with sphericity (Figs. 8 and 11). A new correlation based on circularity measures and vesicularity of particles, Eq. (6), was found that could estimate sphericity of particles with an average error of 4.6% (Fig. 12).
- The best strategies to evaluate 3D parameters indirectly (i.e. volume, surface area, sphericity), are those based on 2D variables with average errors of 2.4–4.6% (Fig. 12). Estimations of 3D parameters based on 1D variables only are associated with higher average errors (between 3.1–7.2%) and, if used, maximum errors up to 50% have to be considered. Out of all correlations found for estimating 3D parameters from 1D and 2D variables, those related to sphericity have highest average errors. We can conclude that sphericity is the most challenging parameter to be estimated from 1D and 2D variables. Correlations summarized in Table 4 and associated uncertainties shown in Fig. 12 provide various solutions and fundamental insights for applications when 3D parameters need to be evaluated indirectly.
- Based on a correlation matrix (Fig. 8), it was found that all the form factors (i.e. 1D shape descriptors) are strongly correlated with either elongation or flatness. Therefore, they can be replaced with each other in order to reduce number of shape descriptors for characterizing particle shape.

Nomenclature

A	Projection area [L^2], see Fig. 3
D_i	Diameter of the largest inscribed circle [L], see Fig. 3
D_c	Diameter of the smallest circumscribed circle [L], see Fig. 3
d_A	Arithmetic average of form dimensions ($=(L+I+S)/3$), [L]
d_{eq}	Spherical equivalent diameter ($=\sqrt[3]{6\ V/\pi}$), [L]
d_G	Geometric average of form dimensions ($=\sqrt[3]{LIS}$), [L]
d_{2D}	Circle equivalent diameter [L], see Fig. 3
$\overline{d_{2D}}$	d_{2D} averaged over 1000 projections [L]
e	Elongation, see Table 3
f	Flatness, see Table 3
F_{Kr}	Krumbein intercept sphericity [50], see Table 3
F_{Cr}	Corey shape factor [55], see Table 3
F_{SF}	Sneed and Folk [1] maximum projection sphericity, see Table 3
F_{Ac}	Aschenbrenner working sphericity [39], see Table 3
F_{WH}	Wilson and Huang shape factor [14], see Table 3
L, I, S	Form dimensions [L], see Fig. 4
l_{min}	Minimum caliper length [L], see Fig. 3
l_{max}	Maximum caliper length [L], see Fig. 3
$max(d_{2D})$	d_{2D} of maximum projection area of the particle [L]
N	Number of projections used for averaging 2D variables
P	Projection perimeter [L], see Fig. 3
r	Pearson's correlation coefficient
SA	Surface area [L^2]
SA_{Cauchy}	Surface area obtained based on Cauchy's theorem [37] [L^2], Eq. (2)
$SA_{\text{ellip.}}$	Ellipsoid surface area [L^2], see Eq. (1)
V	Volume [L^3]
φ_{Cox}	Cox circularity [51], see Table 3
$\overline{\varphi}_{\text{Cox}}$	φ_{Cox} averaged over 1000 projections
φ_{Riley}	Riley circularity [50], see Table 3
$\overline{\varphi}_{\text{Riley}}$	φ_{Riley} averaged over 1000 projections
ψ	Sphericity, see Table 3

Acknowledgment

This research is funded by the Swiss National Science Foundation (SNSF, Grant No. 200020_125024).

References

[1] E.D. Sneed, R.L. Folk, Pebbles in the lower Colorado River, Texas a study in particle morphogenesis, J. Geol. 66 (1958) 114–150.
[2] E.J. Garboczi, Three-dimensional mathematical analysis of particle shape using X-ray tomography and spherical harmonics: Application to aggregates used in concrete, Cem. Concr. Res. 32 (2002) 1621–1638.
[3] O. Kalashnikova, I. Sokolik, Importance of shapes and compositions of wind-blown dust particles for remote sensing at solar wavelengths, Geophys. Res. Lett. 29 (2002) 2–5.
[4] M. Taylor, Quantitative measures for shape and size of particles, Powder Technol. 124 (2002) 94–100.
[5] O. Dubovik, B.N. Holben, T. Lapyonok, A. Sinyuk, M.I. Mishchenko, P. Yang, et al., Non-spherical aerosol retrieval method employing light scattering by spheroids, Geophys. Res. Lett. 29 (2002) 3–6.
[6] L. Banta, K. Cheng, J. Zaniewski, Estimation of limestone particle mass from 2D images, Powder Technol. 132 (2003) 184–189.
[7] C. Riley, W. Rose, G. Bluth, Quantitative shape measurements of distal volcanic ash, J. Geophys. Res. 108 (2003) 1–15.
[8] G. Vallebuona, K. Arburo, A. Casali, A procedure to estimate weight particle distributions from area measurements, Miner. Eng. 16 (2003) 323–329.
[9] M.a. Taylor, E.J. Garboczi, S.T. Erdogan, D.W. Fowler, Some properties of irregular 3-D particles, Powder Technol. 162 (2006) 1–15.
[10] O. Ersoy, E. Aydar, A. Gourgaud, H. Bayhan, Quantitative analysis on volcanic ash surfaces: application of extended depth-of-field (focus) algorithm for light and scanning electron microscopy and 3D reconstruction, Micron 39 (2008) 128–136.
[11] M. Matzl, M. Schneebeli, Stereological measurement of the specific surface area of seasonal snow types: comparison to other methods, and implications for mm-scale vertical profiling, Cold Reg. Sci. Technol. 64 (2010) 1–8.
[12] F. Alfano, C. Bonadonna, P. Delmelle, L. Costantini, Insights on settling velocity from morphological observations, J. Volcanol. Geotherm. Res. 208 (2011) 86–98.
[13] G.H. Bagheri, C. Bonadonna, I. Manzella, P. Pontelandolfo, P. Haas, Dedicated vertical wind tunnel for the study of sedimentation of non-spherical particles, Rev. Sci. Instrum. 84 (2013) 054501.
[14] L. Wilson, T. Huang, The influence of shape on the atmospheric settling velocity of volcanic ash particles, Earth Planet. Sci. Lett. 44 (1979) 311–324.
[15] C. Bonadonna, Thickness variations and volume estimates of tephra fall deposits: the importance of particle Reynolds number, J. Volcanol. Geotherm. Res. 81 (1998) 173–187.
[16] P. Dellino, D. Mele, R. Bonasia, G. Braia, L. La Volpe, R. Sulpizio, The analysis of the influence of pumice shape on its terminal velocity, Geophys. Res. Lett. 32 (2005) 2–5.
[17] S. Scollo, M. Coltelli, F. Prodi, M. Folegani, S. Natali, Terminal settling velocity measurements of volcanic ash during the 2002–2003 Etna eruption by an X-band microwave rain gauge disdrometer, Geophys. Res. Lett. 32 (2005) L10302.
[18] M. Coltelli, L. Miraglia, S. Scollo, Characterization of shape and terminal velocity of tephra particles erupted during the 2002 eruption of Etna volcano, Italy, Bull. Volcanol. 70 (2008) 1103–1112.
[19] P. Delmelle, F. Villieras, M. Pelletier, Surface area, porosity and water adsorption properties of fine volcanic ash particles, Bull. Volcanol. 67 (2005) 160–169.
[20] C.J. Horwell, I. Fenoglio, K. Vala Ragnarsdottir, R.S.J. Sparks, B. Fubini, Surface reactivity of volcanic ash from the eruption of Soufrière Hills volcano, Montserrat, West Indies with implications for health hazards, Environ. Res. 93 (2003) 202–215.
[21] C.J. Horwell, P.J. Baxter, The respiratory health hazards of volcanic ash: a review for volcanic risk mitigation, Bull. Volcanol. 69 (2006) 1–24.
[22] W.I. Rose, A.J. Durant, El Chichón volcano, April 4, 1982: volcanic cloud history and fine ash fallout, Nat. Hazards 51 (2008) 363–374.
[23] W.I. Rose, A.J. Durant, Fine ash content of explosive eruptions, J. Volcanol. Geotherm. Res. (2009) 1–8.
[24] a.J. Durant, C. Bonadonna, C.J. Horwell, Atmospheric and environmental impacts of volcanic particulates, Elements 6 (2010) 235–240.
[25] N.A. Krotkov, D.E. Flittner, A.J. Krueger, A. Kostinski, C. Riley, W. Rose, et al., Effect of particle non-sphericity on satellite monitoring of drifting volcanic ash clouds, J. Quant. Spectrosc. Radiat. Transf. 63 (1999) 613–630.

[26] H. Lindqvist, T. Nousiainen, E. Zubko, O. Muñoz, Optical modeling of vesicular volcanic ash particles, J. Quant. Spectrosc. Radiat. Transf. 112 (2011) 1871–1880.
[27] C.L. Lin, J.D. Miller, 3D characterization and analysis of particle shape using X-ray microtomography (XMT), Powder Technol. 154 (2005) 61–69.
[28] O. Ersoy, E. Şen, E. Aydar, İ. Tatar, H.H. Çelik, Surface area and volume measurements of volcanic ash particles using micro-computed tomography (micro-CT): a comparison with scanning electron microscope (SEM) stereoscopic imaging and geometric considerations, J. Volcanol. Geotherm. Res. 196 (2010) 281–286.
[29] O.P. Mills, W.I. Rose, Shape and surface area measurements using scanning electron microscope stereo-pair images of volcanic ash particles, Geosphere 6 (2010) 805–811.
[30] D. Asahina, M.a. Taylor, Geometry of irregular particles: direct surface measurements by 3-D laser scanner, Powder Technol. 213 (2011) 70–78.
[31] E.J. Garboczi, X. Liu, M.a. Taylor, The 3-D shape of blasted and crushed rocks: from 20 μm to 38 mm, Powder Technol. 229 (2012) 84–89.
[32] O. Ersoy, Surface area and volume measurements of volcanic ash particles by SEM stereoscopic imaging, J. Volcanol. Geotherm. Res. 190 (2010) 290–296.
[33] H. Wadell, Volume, shape, and roundness of rock particles, J. Geol. 40 (1932) 443–451.
[34] S. Blott, K. Pye, Particle shape: a review and new methods of characterization and classification, Sedimentology 55 (2008) 31–63.
[35] W.C. Krumbein, Measurement and geological significance of shape and roundness of sedimentary particles, J. Sediment. Res. 11 (1941) 64–72.
[36] C. Bonadonna, R. Cioni, M. Pistolesi, C. Connor, S. Scollo, L. Pioli, et al., Determination of the largest clast sizes of tephra deposits for the characterization of explosive eruptions: a study of the IAVCEI commission on tephra hazard modelling, Bull. Volcanol. 75 (2013) 680.
[37] A.L. Cauchy, Mémoire sur la rectification des courbes et la quadrature des surfaces courbées, 1832.
[38] A. Laurentini, How many 2D silhouettes does it take to reconstruct a 3D object? Comput. Vis. Image Underst. 67 (1997) 81–87.
[39] B.C. Aschenbrenner, A new method of expressing particle sphericity, J. Sediment. Res. 26 (1956) 15.
[40] D. Kunii, O. Levenspiel, Bubbling bed model, Model for flow of gas through a fluidized bed, ACS Publications, 1968.
[41] Z. Zhang, J. Yang, L. Ding, Y. Zhao, An improved estimation of coal particle mass using image analysis, Powder Technol. 229 (2012) 178–184.
[42] S. Biass, C. Bonadonna, A quantitative uncertainty assessment of eruptive parameters derived from tephra deposits: the example of two large eruptions of Cotopaxi volcano, Ecuador, Bull. Volcanol. 73 (2011) 73–90.
[43] F. Barberi, M. Coltelli, a. Frullani, M. Rosi, E. Almeida, Chronology and dispersal characteristics of recently (last 5000 years) erupted tephra of Cotopaxi (Ecuador): implications for long-term eruptive forecasting, J. Volcanol. Geotherm. Res. 69 (1995) 217–239.
[44] L. Costantini, B.F. Houghton, C. Bonadonna, Constraints on eruption dynamics of basaltic explosive activity derived from chemical and microtextural study: the example of the Fontana Lapilli Plinian eruption, Nicaragua, J. Volcanol. Geotherm. Res. 189 (2010) 207–224.
[45] P. Vonlanthen, J. Rausch, R.A. Ketcham, B. Putlitz, L.P. Baumgartner, B. Grobety, SEM micro-computed tomography (SEM micro-CT): a new method for high-resolution 3D analyses of small volcanic ash particles, J. Volcanol. Geotherm. Res. (2014) (submitted for publication).
[46] B. Pauwels, X. Liu, A. Sasov, X-ray nanotomography in a SEM, Proc. SPIE 7804, Dev. X-Ray Tomogr. VII, 2010 (78040S–78040S–8).
[47] C.A. Schneider, W.S. Rasband, K.W. Eliceiri, NIH Image to ImageJ: 25 years of image analysis, Nat. Methods 9 (2012) 671–675.
[48] RCT, R: A Language and Environment for Statistical Computing, http://www.r-project.org 2014.
[49] J. Korsawe, Minimal Bounding Box, http://www.mathworks.com/matlabcentral/fileexchange/18264-minimal-bounding-box 2008.
[50] N.A. Riley, Projection sphericity, J. Sediment. Res. 11 (1941) 94–95.
[51] E.P. Cox, A method of assigning numerical and percentage values to the degree of roundness of sand grains, J. Paleontol. 1 (1927) 179–183.
[52] E. Loth, Drag of non-spherical solid particles of regular and irregular shape, Powder Technol. 182 (2008) 342–353.
[53] T. Zingg, Beitrag zur Schotteranalyse : die Schotteranalyse und ihre Anwendung auf die Glattalschotter, Schweiz. Mineral. Petrogr. Mitt. 15 (1935) 39–40.
[54] W.C. Krumbein, F. Pettijohn, Manual of Sedimentary Petrology, Century and Crofts, New York, 1938.
[55] A.T. Corey, Influence of Shape on the Fall Velocity of Sand Grains, Audio Visual Service, Colorado State University, 1963.
[56] E.E. Underwood, Quantitative Stereology, Wesley Publishing Co, Reading, Mass, 1970.
[57] H. Wadell, Volume, shape, and roundness of quartz particles, J. Geol. (1935) 250–280.